Materials Today Chemistry 55 (2026) 103789

Contents lists available at ScienceDirect

Materials Today Chemistry

journal homepage: www.journals.elsevier.com/materials-today-chemistry/

Magnesium- and cerium-doped mesoporous bioactive glasses as multifunctional platform for polyphenol delivery and enhanced antioxidant activity

Chiara Cavazzoli [a,1], Ranveer Kaur [b,1], Ksenia Menshikh [c,d], Chiara Grassi [a], Alfonso Zambon [a], Lia Rimondini [b], Andrea Cochis [b,*], Gigliola Lusvardi [a,**]

[a] Department of Chemical and Geological Sciences, University of Modena and Reggio Emilia, Modena, 41125, Italy
[b] Center for Translational Research on Autoimmune and Allergic Disease—CAAD, Department of Health Sciences, Università del Piemonte Orientale, Novara, 28100, Italy
[c] CÚRAM, Research Ireland Centre for Medical Devices, Galway, Ireland
[d] School of Engineering, College of Science and Engineering, University of Galway, Galway, Ireland

ARTICLE INFO

Keywords:
Mesoporous bioactive glasses
Cerium doping
Magnesium doping
Polyphenols
Antioxidant activity

ABSTRACT

Mesoporous bioactive glasses (MBGs) represent a promising class of materials for biomedical applications due to their large surface area, high pore volume, and tuneable composition.

Due to such surface properties, this work explores for the first time the possibility of exploiting MBGs as a multifunctional platform boosting bioactivity by magnesium and cerium co-doping, as well as a delivery of polyphenols, with the aim of tuning inflammation in situ.

Accordingly, four MBG compositions with varying Mg and Ce contents were synthesized via the sol–gel method and loaded with three pure polyphenols: 3-hydroxyflavone, quercetin, and morin hydrate. The multiparametric characterization confirmed the amorphous nature of all glasses, high specific surface area (SSA, > 300 m^2/g), *in vitro* bioactivity in simulated body fluid (SBF), significant antioxidant activity, and cytocompatibility toward human bone marrow-derived mesenchymal stem cells (hBMSCs), as well. In particular, Ce/Mg co-doping notably enhanced catalase (CAT)-like activity, while polyphenol loading, particularly with quercetin, markedly improved superoxide dismutase (SOD)-mimetic activity. Similarly, quercetin functionalization demonstrated strong scavenging activity, protecting hBMSCs from the intracellular accumulation of toxic reactive oxygen species (ROS) compared with bulk controls when oxidative stress was induced with H_2O_2. Moreover, when the pro-inflammatory cascade was induced by interleukin administration, the presence of quercetin effectively promoted the upregulation of the anti-inflammatory genes TGF-β1 and IL-10, demonstrating a strong ability to modulate the inflammation in situ. Taken together, these findings highlight the potential of Ce/Mg co-doped MBGs as bioactive multifunctional carriers for the delivery of antioxidant biomolecules.

1. Introduction

Biomaterials are natural or synthetic materials that promote healing and facilitate the reconstruction of damaged body tissues [1,2]. Among them, bioceramics, particularly bioactive glasses (BGs), are widely used for biomedical applications due to their non-toxic nature, biocompatibility, and chemical stability in biological environments [3]. Additionally, some biomaterials can degrade over time and be gradually replaced by newly regenerated tissue [4,5]. The incorporation of therapeutic inorganic ions (TIIs) into the structure of BGs further enhances their biofunctionality, imparting properties such as angiogenesis, osteogenesis, cementogenesis, and bactericidal activity [6–8]. Our previous studies have focused on mesoporous bioactive glasses (MBGs) [9–13], a subclass of BGs particularly well-suited for drug delivery systems (DDSs) due to their high pore volume, large specific surface area (SSA), and well-ordered structure. These characteristics enable the efficient loading

* Corresponding author.
** Corresponding author.
E-mail addresses: andrea.cochis@med.uniupo.it (A. Cochis), gigliola.lusvardi@unimore.it (G. Lusvardi).
[1] These authors contributed equally to this work.

https://doi.org/10.1016/j.mtchem.2026.103789
Received 11 March 2026; Received in revised form 9 June 2026; Accepted 11 June 2026
Available online 18 June 2026

Table 1
Theoretical composition (mol %) of the studied MBGs.

MBGs	SiO_2	CaO	P_2O_5	CeO_2	MgO
MBG3.6-Mg	77.1	14.5	4.8	-	3.6
MBG5.3-Mg	75.8	14.2	4.7	-	5.3
MBG3.6-Ce/Mg	77.1	14.5	4.8	1.8	1.8
MBG5.3-Ce/Mg	75.8	14.2	4.7	2.65	2.65

of small organic molecules aimed at improving MBGs bioactivity, as well as their controlled release in situ in order to obtain multifunctional platforms [14,15]. Previously, we have extensively investigated the doping of MBGs with cerium (MBGs-Ce), chosen for its antitumor, anti-inflammatory, and antioxidant properties [7,16,17]. Importantly, we have demonstrated that cerium does not inhibit the bioactivity of MBGs, allowing its therapeutic benefits to be harnessed without compromising their bone regeneration potential [10–12,18]. Interestingly, while cerium is often associated with antimicrobial properties in the literature [19], our findings indicate that MBGs-Ce do not exhibit significant antibacterial activity [19]. Building on these findings, we recently explored the introduction of a second antimicrobial dopant ion, specifically copper, silver, and zinc. Our results suggest that MBGs-Ce/Cu and MBGs-Ce/Ag hold promise as multifunctional materials for biomedical applications, offering targeted antimicrobial effects alongside additional therapeutic benefits, confirming the hypothesis to apply MBGs as multifunctional platform for the delivery of ions combining different biological properties [20].

In this study, we further expanded the investigation of MBGs as multifunctional delivery platform by introducing magnesium as a second dopant ion to further enhance the biological performance of MBGs. In fact, as largely reported by literature magnesium is an essential intracellular alkaline earth metal primarily stored in bones and soft tissues such as muscles [21–23]. It plays a crucial role in numerous enzymatic reactions, including energy metabolism, nucleic acid and protein synthesis, and active calcium transport [21,23]. Additionally, Mg is vital for living cells due to its interaction with phosphate ions, as ATP typically exists in cells as a chelate with Mg^{2+} [6]. It also acts as a cofactor for many enzymes, facilitating catalytic activity [6,24]. Mg deficiency has been linked to various pathological conditions, including malabsorption syndrome, renal dysfunction, and hormonal imbalances [23,24]. In bone health, magnesium contributes to osteoporosis treatment and bone repair by reducing fracture risk and enhancing bone density [21,25]. This effect is mediated through its ability to inhibit osteoclast function while stimulating osteoblast activity [21,25,26]. Furthermore, Mg^{2+} ions are essential for cytoskeletal integrity, skeletal tissue development, bone remodelling, and the activation of phagocytosis [21].

In parallel, Fare clic o toccare qui per immettere il testo.the functionalization of MBGs with natural compounds was explored in this work as a promising strategy to release in situ anti-inflammatory and anti-oxidant molecules as alternative to conventional systemic administration as suggested by some literature to enhance tissue healing [27–29]. Among these, polyphenols have attracted significant interest due to their antioxidant, anti-inflammatory, antibacterial, osteoinductive and anticancer properties [30–34].

Based on these premises, the present study aims to identify hybrid bioactive and multifunctional materials with optimized antioxidant properties and drug delivery. To this end, we conducted a multiparametric evaluation of MBGs-Mg and MBGs-Ce/Mg loaded with three different biomolecules: 3-hydroxyflavone, quercetin and morin hydrate. Finally, the most promising system based on MBGs-Ce/Mg functionalized with quercetin was tested for its antioxidant and anti-inflammatory properties towards human bone-marrow derived mesenchymal stem cells (hBMSCs), which were selected as representative model for cells involved in the healing process under pro-inflammatory conditions.

2. Materials and methods

2.1. MBGs preparation and characterization techniques

SiO_2-CaO-P_2O_5-MgO and SiO_2-CaO-P_2O_5-CeO_2-MgO glasses were synthesized by the sol-gel EISA method using tetraethyl orthosilicate (TEOS), triethyl phosphate (TEP), $Ca(NO_3)_2{\cdot}4H_2O$, $Ce(NO_3)_3{\cdot}6H_2O$ and $Mg(NO_3)_2{\cdot}6H_2O$ as precursors and P123 as structure directing aget [7,10–12,35]. The optimized sample compositions are shown in Table 1; the mixture was stirred for 24 h and poured into Petri dishes until solvent evaporation and gelling. The dried gels were calcined at 700°C for 3 h under air atmosphere. The resultant powder was sieved to a particle size range of 355-212 μm.

In each formula reported in Table 1, the number associated with each MBG corresponds to the total number of moles of modifier oxide(s) added, and when two ions are both present the ratio is 1:1.

2.1.1. X-Ray Powder Diffraction (XRPD)

X-Ray Powder Diffraction (XRPD) was used to evaluate the possible formation of secondary phases induced by the addition of dopant ions. The evaluations were carried out using an Empyrean MultiCore 3rd generation (Malvern Panalytical, Malvern, United Kingdom) diffractometer.

2.2. In vitro cytocompatibility assay

For assessing the preliminary cytocompatibility of the MBGs, they were tested in direct contact with human bone-marrow derived mesenchymal stem cells (hBMSCs), as well as in an extract-based assay. To perform these tests, the powder was compacted into disks with a diameter of 1 cm. Each disk was prepared using 90 mg of powder and a uniaxial pressing force of 10^5 N; this solution was considered for the biological characterization following the strategy in our previous work [36], and the potential limitations derived by the use of powders as recently reported by the authors [37].

Firstly, the MBG disks were sterilized by incubation at 160 °C for 2 hours, cooled down and quickly washed with sterile phosphate-buffered saline (PBS). The sterilized and washed disks were then arranged in the wells of a 24-well standard culture plate and immersed overnight in culture medium consisting of low-glucose (1 g/L) Dulbecco's modified Eagle's medium (DMEM, Sigma-Aldrich, USA) supplemented with 15% fetal bovine serum (FBS, Sigma-Aldrich, USA) and 1% penicillin-streptomycin (PS, Invitrogen, USA).

For the experiments, hBMSCs (hTERT-BMSC clone Y201, immortalized through hTERT lentiviral vectors [38] were cultured in low-glucose DMEM supplemented with 10% FBS and 1% PS until 80-90% confluence (37 °C, humidified atmosphere, 5% CO_2), detached by trypsin-EDTA (1X, Sigma-Aldrich, USA) solution, and harvested. For the extract-based experiment, the cells were seeded in the amount of $2.0x10^4$ cells per well of a standard 24-well plate, and cultured in an MBG-conditioned medium, exchanged for a 24-h extract and a 48-h extract in the following days. For the direct-contact experiment, the cells were seeded onto the MBG disks at a density of $2.0x10^4$ cells per disk and kept in standard conditions for 3 days with culture medium changed daily. The medium exposed to cell-seeded MBGs was collected for the following ion release analysis described in the respective section.

2.2.1. Cell metabolic activity assay

To evaluate the metabolic activity of cells in contact with the MBGs samples, Alamar blue solution (alamarBlue™ HS Cell Viability Reagent, Invitrogen, USA) in culture medium was added to the samples. After a 3-h incubation in the dark, 100 μL of the supernatant was transferred into a black opaque 96-well plate and read with a spectrophotometer (Spark®, Tecan Trading AG, CH) using an excitation wavelength of 560 nm, and an emission wavelength of 590 nm. Results were presented in relative fluorescent units (RFU).

2.2.2. Cell morphology assay

To analyse the morphology of hBMSCs cultured in direct contact with MBG disks, scanning electron microscopy (SEM) was used. The samples were fixed in 2.5% glutaraldehyde (prepared from 25% solution (Merck KGaA, Germany)) for 30 min at RT, then washed with PBS to remove fixative, and dehydrated using graded ethanol series (30, 50, 70, 90, 95, and 100%, 20 minutes each). Subsequently, the specimens were submerged in hexamethyldisilazane (HMDS, Alfa Aesar, USA) and left to air-dry overnight. The dehydrated samples were mounted onto aluminium stubs using conductive carbon tape, coated with a 10 nm gold layer (DII-29019SCTR SmartCoater, Jeol, Japan), and examined using a scanning electron microscope (JSM-IT500 InTouchScope™, Jeol, Japan).

2.3. Dissolution studies

The dissolution in SBF after 7, 14, and 30 days was evaluated by quantifying the release of silicon, calcium, phosphorus, cerium, and magnesium. Elemental analysis was performed using an Agilent 6410 Triple Quadrupole LC/MS system. Furthermore, the culture medium collected from cell-seeded MBGs was analysed to determine the release of Ce and Mg ions after the incubation period (1-2-3 days).

2.4. Loading with polyphenols

In this study, we used a 1.0 mg/mL loading solution of the following polyphenols: 3-hydroxyflavone (F), quercetin (Q), and morin hydrate (M); F, Q, and M are 98, 95, and 100% pure, respectively. The loading solutions were prepared by dissolving polyphenols in ethanol for 1 h under magnetic stirring. As reported, the loading process involved the soaking 0.1 g of each sample in 5 mL of loading solution for 3 hours at 37 °C. To prevent light exposure, all samples were wrapped in aluminium foil [10,12,18].

2.4.1. Elemental analyses (AE)

Elemental analysis (EA) was carried out with a FLASH 2000 Thermo Fischer analyser in order to quantify the amount of biomolecules in the loaded MBGs by measuring C (%). The results for each biomolecule are expressed as loading content, LC (%), and loading efficiency, LE (%), calculated as follows, where m = mass.

$$\mathrm{LC}(\%) = \frac{\mathrm{MM(biomolecule)}}{\mathrm{mol\ (C\ into\ biomolecule)\ x\ MA(C)}} \times \mathrm{C}(\%)$$

$$\mathrm{LE}(\%)^{*} = \frac{\mathrm{m}_{(\mathrm{biomolecule\ loaded})}{}^{*}}{\mathrm{m\ (biomolecule\ loading\ solution)}} \times 100$$

* *Derived from LC(%).*

2.4.2. Specific surface area determination (SSA)

The specific surface area (SSA) was evaluated before and after loading to assess potential textural changes resulting from the introduction of dopant ions or biomolecules. SSA was determined by nitrogen adsorption using a Micromeritics Chemisorb 2750 instrument and the Brunauer-Emmett-Teller (BET) method.

2.5. Antioxidant activity assay

The antioxidant properties of each MBG and loaded-MBG were evaluated by enzymatic assays as their ability to remove the hydrogen peroxide (H_2O_2, CAT-like activity) and radical superoxide anion (O_2^-, SOD-like activity), two of the most significant reactive oxygen species (ROS) [7,39–41].

2.5.1. Catalase (CAT)-like activity

The tests were performed using the Fluorimetric Hydrogen Peroxide Assay Kit from Sigma Aldrich with a TECAN GeniosPro microplate reader, as presented in our previous paper. The presence of H_2O_2 is detected in SBF through its reaction (1:1 stoichiometry ratio) with a molecular probe catalysed by the peroxidase enzyme, which generates a red fluorescent product that can be analysed fluorometrically. We suspended 40 mg of each MBG in 400 μL of a 50 μM solution of H_2O_2 in SBF and measured the residual concentration of H_2O_2 by the Amplex assay after 30 and 120 min of soaking. CAT activity is reported as the percentage of H_2O_2 decomposed at the end of the assay.

2.5.2. Superoxide dismutase (SOD)-like activity

The tests were performed using the SOD Determination Kit (Sigma Aldrich) adapted for a UV–Vis Spectrophotometer (JASCO V-570, Mettler Toledo, Columbus, Ohio, United States). In this assay, the SOD-like activity is expressed as the rate of inhibition (I.R.%) of the formation of a water-soluble formazan dye formed upon reduction of a tetrazolium salt (WST-1) by the superoxide anion catalysed by Xanthine Oxidase (XO) and inhibited by SOD.

The SOD assay was performed including material-specific blank corrections. For sample preparation, 200 μL of WST-1 working solution, 20 μL of enzyme solution, and 20 mg of sample were added into an Eppendorf tube. The corresponding sample blank was prepared by replacing the enzyme solution with 20 μL of dilution buffer while maintaining the same amount of sample (20 mg). Both sample and blank solutions were incubated at 37 °C for 30 min. After incubation, 150 μL of each solution were collected and diluted with 100 μL of bidistilled water prior to UV–Vis analysis.

In addition, a reference control corresponding to the maximum theoretical formation of formazan in the absence of material was prepared, together with its related blank. The reference solution consisted of 200 μL of WST-1 working solution, 20 μL of enzyme solution, and 20 μL of dilution buffer, whereas the corresponding blank contained 200 μL of WST-1 working solution and 40 μL of dilution buffer. These solutions underwent the same incubation and dilution procedure before UV–Vis measurements.

To calculate the SOD activity of the materials, the following equation was used:

$$\textit{SOD activity}\ (I.R.\%) = \frac{A_{ref}\ (440\ nm) - A_{sample}\ (440\ nm)}{A_{ref}\ (440\ nm)} \cdot 100$$

The absorbance values obtained from the material-specific blanks were subtracted from the corresponding sample measurements to minimize contributions from sample turbidity, intrinsic absorbance of released compounds, and other non-specific optical interferences.

2.6. In vitro bioactivity assessment in simulated body fluid (SBF)

All samples were soaked in simulated body fluid (SBF) at 37°C for 7, 14, and 30 days to verify the formation of an apatite layer, mainly composed of $Ca_{10}(PO_4)_6(OH)_2$ (hydroxyapatite, HA) [42,43]. After soaking, Fourier transform infrared (FT-IR) spectra were collected on a PerkinElmer 1600 spectrometer in the range of 400-4000 cm^{-1} to identify the characteristic bands of HA. Moreover, mineralogical evaluations by X-Ray Powder Diffraction (XRPD) were also carried out using an X'Pert PRO-PANAnalytical diffractometer in order to detect the characteristic peaks of HA. Scanning Electron Microscopy (SEM) (JEOL JSM-6010LA microscope, equipped with Energy Dispersive Spectroscopy, EDS, Leica Microsystems Wetzlar, Germany) was used to evaluate morphological changes on the surface.

2.7. In vitro biological assays of quercetin-loaded MBGs

Following the assessment of polyphenols loading efficiency, *in vitro* anti-oxidant activity, and bioactivity, the quercetin-loaded MBG disks were selected as the most promising specimens for a further biological characterization due to their superior loading efficiency and their ability

to maintain >83% of SOD like activity. The subsequent analyses aimed to assess post-loading cytocompatibility and the potential antioxidant and anti-inflammatory effects of the incorporated quercetin. The disks were fabricated according to the protocol in section 2.2. Prior to seeding, the disks underwent sterilisation via UV irradiation, to prevent the degradation of quercetin, for 1 hour per side and were subsequently transferred into 24-well culture plates. The hBMSCs were cultured the same way as mentioned in section 2.2 and were seeded directly at a density of 2 x10^4 cells per well on the quercetin-loaded disks. Following a 3-h pre-adhesion step, 1 mL complete low-glucose DMEM (section 2.2) was added, and the plates were incubated at 37°C and the culture medium was replaced every 3 days. Cells cultured directly on the polystyrene surface served as the control group in all the evaluations. All experimental procedures were performed in triplicate to ensure reproducibility.

2.7.1. Cytocompatibility assessment

For the metabolic evaluation of the hBMSCs seeded on quercetin-loaded MBG disks, the AlamarBlue assay was performed as mentioned in section 2.2.1. Data were collected at 1, 2 and 3 days of cultivation; results were plotted as relative fluorescence units (RFU) and normalized against control to determine percentage metabolic activity. In addition to metabolic activity, to assess the cytotoxicity of the quercetin-loaded MBGs, supernatants were collected at the same time-points and evaluated via LDH assay (CyQuant LDH cytotoxicity assay, Invitrogen, USA) according to the manufacturer's instructions. To provide visual data of the specimens-adhered cells, samples were stained with NucBlue reagent (Invitrogen, USA) in order to visualize the nuclei of the cells colonizing the specimens; fluorescent images were collected with a confocal Leica THUNDER imaging system and further processed with ImageJ software. Moreover, hBMSCs cultured in direct contact with quercetin-loaded MBG disks was characterized using SEM as described before (section 2.2.2) and complemented by EDS, for elemental surface mapping.

2.7.2. Antioxidant activity analysis

To evaluate the antioxidant potential of the quercetin-loaded MBG disks, the cell-seeded disks were exposed to a 50 μM H_2O_2 doped media for 48 hours to simulate a pro-oxidative stress environment. Following the incubation, the medium was aspirated, and the disks were rinsed with PBS. Intracellular ROS levels were detected using CellROX™ Green Reagent (C10444, Invitrogen, USA) according to the manufacturer's protocol. This fluorogenic probe remains non-fluorescent until oxidation by ROS, at which point it binds to DNA and emits a stable fluorescent signal detectable at 525 nm following excitation with a 488 nm laser. For nuclear visualization, the samples were counterstained with NucBlue™ for 30 minutes, followed by a final PBS wash to eliminate unbound dye. Fluorescence imaging was performed using a Leica THUNDER microscope. Quantitative analysis was conducted via ImageJ software to determine the mean fluorescence intensity.

2.7.3. Anti-inflammatory response analysis

To investigate the anti-inflammatory potential, the hBMSCs-seeded disks were cultivated in a simulated pro-inflammatory environment by introducing into the culture medium a cytokine cocktail consisting of 20 ng/mL TNF-α and 10 ng/mL IL-1β for 48 hours. Post-incubation, the conditioned media were removed, and the disks were rinsed thoroughly with PBS. Total RNA was isolated by adding 500 μL of TRIzol™ Reagent (Thermo Fisher Scientific, USA) per well; following a 15-min lysis period, the lysates were transferred to 2 mL microcentrifuge tubes and processed according to the manufacturer's instructions. The purity and concentration of the extracted RNA were determined, and subsequent cDNA synthesis was performed using the Verso cDNA Synthesis Kit (Thermo Scientific, USA). The reaction mixture was prepared using SYBR green master mix (Applied Biosciences, 4472942, USA), cDNA, and specific primers (Integrated DNA Technologies, USA) as per the manufacturer's protocol. Finally, real-time PCR (RT-qPCR) was applied to determine the expression of the pro- and anti-inflammatory genes CXCL8, TNF-α, IL-10, and TGF-β1; primers and probes are listed in Table 2. All the results were normalized with GADPH chosen as a housekeeping gene.

Table 2
Sequence of Forward and Reverse primers used for RT-qPCR reaction.

Gene	Forward Primer	Reverse Primer
CXCL8	TTGCCAAGGAGTGCTAAAG	CACTCTCAATCACTCTCAGTT
TNF- α	CTGGTATGAGCCCATCTATCT	GGGCAATGATCCCAAAGTAG
IL-10	TCCTTGCTGGAGGACTTTA	ATGTCTGGGTCTTGGTTCT
TGF-β1	GAC AGC AGG GAT AAC ACA C	CCA TGA GAA GCA GGA AAG G
GAPDH	GTATGACAACAGCCTCAAGAT	GTCCTTCCACGATACCAAAG

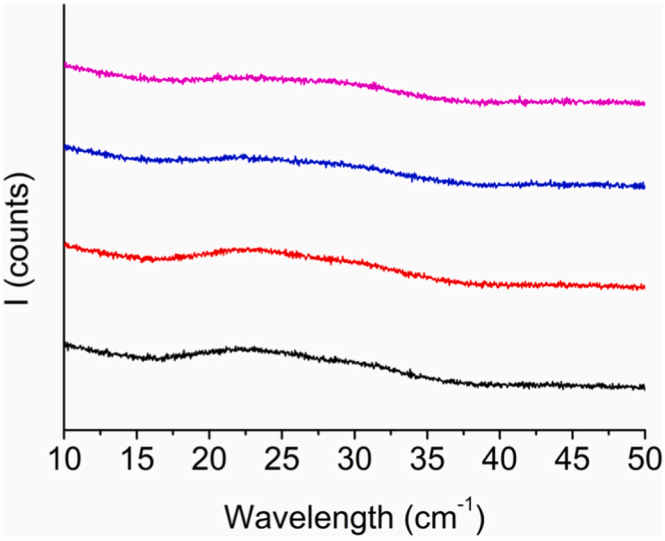

Fig. 1. XRPD patterns of: MBG3.6-Mg (black), MBG5.3-Mg (red), MBG3.6-Ce/Mg (blue), MBG5.3-Ce/Mg (pink).

2.8. Statistical analysis

Experiments were performed in triplicate. Data were analysed using GraphPad Prism (version 8.4.2). Statistical significance was determined using one-way or two-way analysis of variance (ANOVA), followed by Tukey's multiple comparisons test to identify specific differences between groups. All results are expressed as mean ± standard deviation (SD) or standard error of mean (SEM), and p-values < 0.05 were considered statistically significant between the compared groups.

3. Results and discussion

3.1. Characterization: XRPD

Fig. 1 reports the XRPD patterns for MBGs-Mg and MBGs-Ce/Mg; all doped samples exhibit an amorphous structure and do not show any diffraction peaks corresponding to a crystalline phase.

3.2. In vitro cytocompatibility assay

To assess the preliminary cytocompatibility of the MBGs, the samples were tested in the form of disks with hBMSCs – in direct contact and indirectly, via extracts.

The metabolic activity of the cells evaluated via the Alamar blue assay demonstrated good cytocompatibility of all tested samples (Fig. 2, a). Although a lower metabolic activity was observed in direct contact

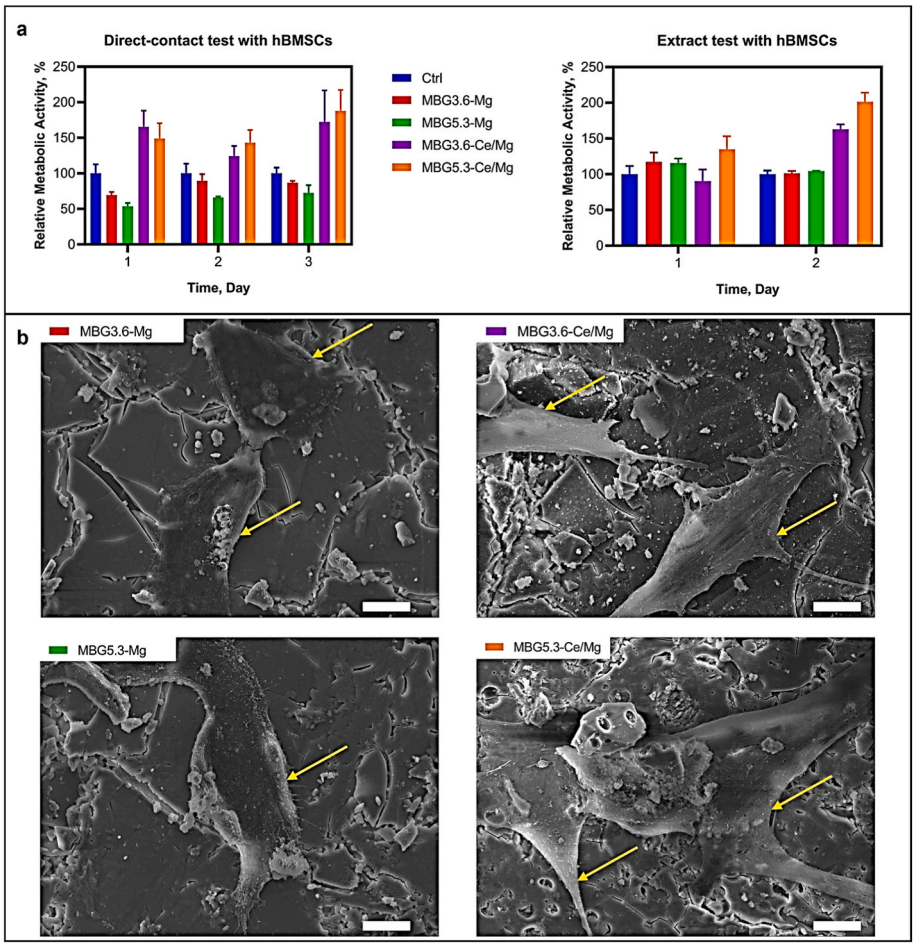

Fig. 2. (a) Metabolic activity of hBMSCs cultured with MBGs in direct contact or with MBG extracts, 'Control' represents hBMSCs cultivated without MBGs or extracts, and the values are presented as mean ± SD of normalized RFU; (b) SEM images of hBMSCs cultivated on the MBG disks, scale bars 10 μm, arrows indicate hBMSCs cells.

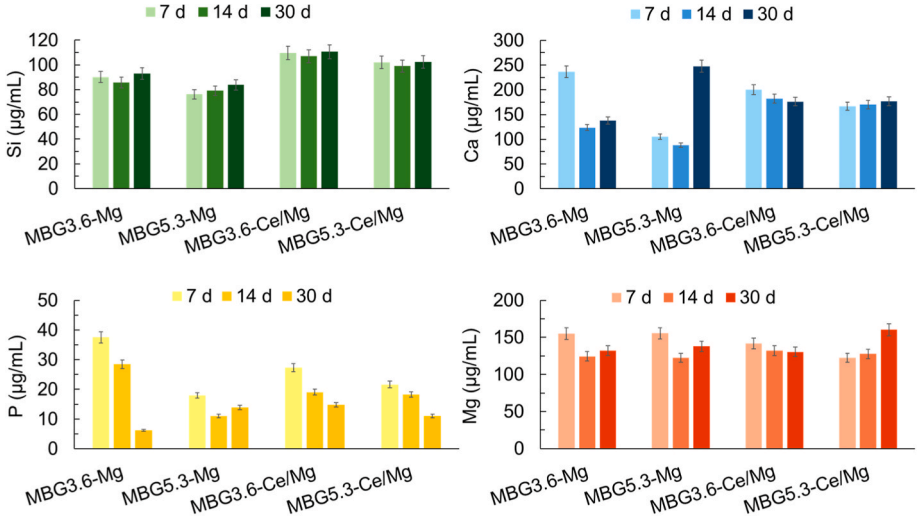

Fig. 3. Releases of silicon, calcium, phosphorous and magnesium after 7, 14 and 30 days in SBF. Tests were performed in triplicate; data are presented as averages with error bars representing the SD.

with MBG3.6-Mg and MBG5.3-Mg during the first two days of the experiment, by the third day, the hBMSCs' metabolic activity exceeded 70% of the control (hBMSCs cultivated in standard conditions without the disks). The metabolic activity of hBMSCs incubated with other MBGs or their extracts was comparable to that of the control group in all three time points tested. Moreover, the samples containing Ce (MBG3.6-Ce/Mg and MBG5.3-Ce/Mg) appeared to enhance the metabolic activity of hBMSCs in both direct-contact and extracts tests, especially at the final

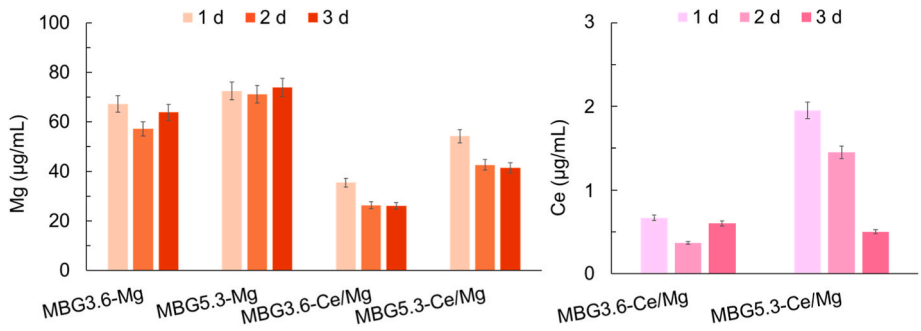

Fig. 4. Releases of magnesium and cerium after 1, 2, and 3 days in the cell culture medium. Tests were performed in triplicate; data are presented as averages with error bars representing the SD.

Table 3
LC (%) and LE (%) of loaded-MBGs calculated by AE.

MBGs	Q	F	M
	LC (LE %)	LC (LE %)	LC (LE %)
MBG3.6-Mg	1.1 (21.3)	0.6 (12.7)	0.5 (9.7)
MBG5.3-Mg	0.7 (14.4)	0.6 (12.7)	0.5 (9.1)
MBG3.6-Ce/Mg	0.9 (18.4)	1.0 (19.3)	0.3 (5.4)
MBG5.3-Ce/Mg	1.3 (26.0)	0.6 (12.2)	0.4 (8.6)

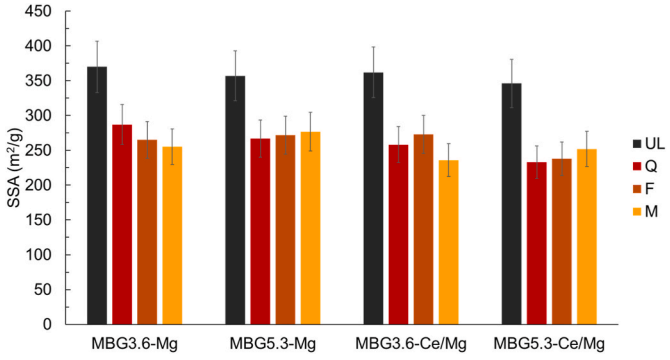

Fig. 5. SSA (m^2/g) of MBGs before and after biomolecule loading. Tests were performed in triplicate. Data are presented as averages, with error bars representing the SD. UL = unloaded.

incubation time points. SEM observations of the hBMSCs-seeded MBG disks revealed well-attached cells exhibiting stretched and flattened morphology with multiple filopodia (Fig. 2, b).

3.3. Dissolution studies

The data presented in Fig. 3 indicate that the release of both Si (90–110 μg/mL) and Mg (122–160 μg/mL) remains relatively constant across different samples and over time. In contrast, the release of Ca appears to be stable in the Ce-doped samples (170–200 μg/mL). However, the MBG3.6-Mg and MBG5.3-Mg samples exhibit different behaviours: the former releases a higher amount of Ca after 7 days (236 μg/mL), whereas the latter shows an increased release after 30 days (248 μg/mL). This distinct trend is consistent with the dissolution/reprecipitation behaviour of MBGs and is associated with the formation of an apatitic phase [9,44]. As for P release, all samples follow a similar trend, with a higher P release observed after 7 days (38–18 μg/mL), followed by comparable values across samples after 30 days (6–15 μg/mL). Ce release remained below 1 μg/mL in all samples (data not shown).

Furthermore, the culture medium collected from the cell-seeded MBGs was analysed by ICP to quantify the release of Ce and Mg ions after 1, 2, and 3 days of incubation (Fig. 4). The Ce release remained very low, around 1–2 μg/mL, similarly to what was observed in SBF. Conversely, Mg release exhibited more pronounced variations among the samples. After contact with the cells, MBG3.6-Mg and MBG5.3-Mg released between 57 and 82 μg/mL of Mg, while the samples containing both Ce and Mg showed roughly half of these values, ranging from 26 to 54 μg/mL.

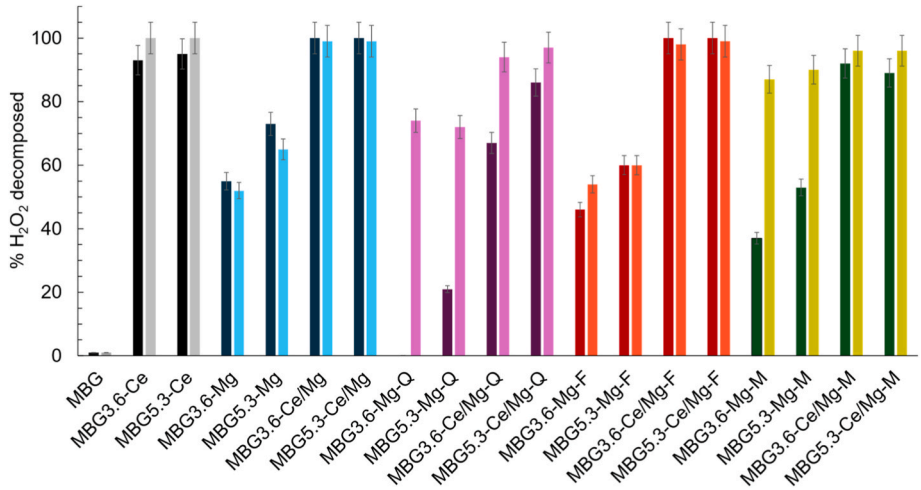

Fig. 6. CAT-like activities expressed as a percentage of decomposed H_2O_2. Dark shade: 30 min; light shade: 120 min. Tests were performed in triplicate; data are presented as averages with error bars representing the SD.

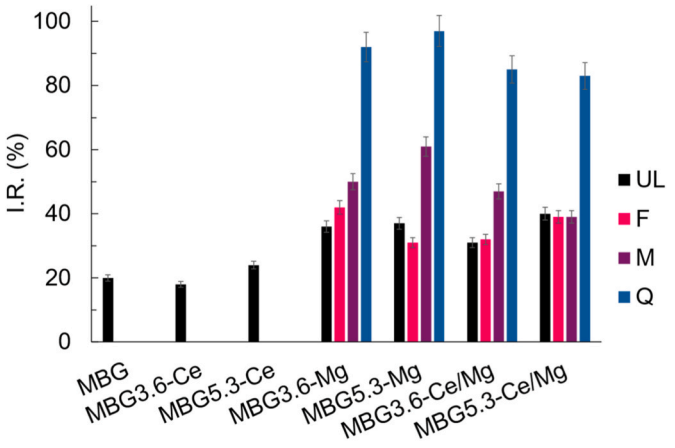

Fig. 7. SOD-like activities expressed as percentages of inhibition rate (I.R. %). UL = unloaded. Tests were performed in triplicate; data are presented as averages with error bars representing the SD.

3.4. Loading evaluations: EA and BET

LC (%) and LE (%) are reported in Table 3; these results indicate a good loading of the selected biomolecules on MBGs. The loading of Q and F aligns with previous studies on MBGs-Ce [12,20], with LC ranging from 0.6 to 1.3% and LE from 12.2 to 26.0%. In contrast, M shows slightly lower values (LC 0.3–0.5%, LE 5.4–9.7%).

Fig. 5 shows that the incorporation of Ce and Mg into the glass does not affect the SSA, an intrinsic characteristic of MBG glasses, which remains high. According to the literature, while pure mesoporous silicas can achieve surface areas exceeding 600 m^2/g [45], the addition of multiple network modifiers and TIIs in BGs inherently modulates these values; nevertheless, an SSA above 100 m^2/g is already classified as exceptionally elevated for multi-component sol-gel systems, crucially accelerating apatite-forming kinetics [46]. Previous studies have reported that the SSA of undoped MBG, as well as MBG3.6-Ce and MBG5.3-Ce, ranges between 300 and 360 m^2/g [11,12], regardless of the cerium content; these results are in line with the values of SSA, obtained in other work [47], using a triblock copolymer as structure directing agent [47]. All unloaded (UL) MBGs-Mg and MBGs-Ce/Mg samples exhibit SSA values exceeding 346 m^2/g. Loaded MBGs showed a significant decrease in SSA, likely due to pore occlusion. After loading with Q, F, and M, SSA values decreased substantially to 236–287 m^2/g.

3.5. Antioxidant activity assay

3.5.1. CAT-like activity

Fig. 6 illustrates the assessment of the CAT-like activity of MBGs and biomolecules-loaded MBGs after 30 minutes (dark shade) and 120 minutes (light shade) of contact. This activity is primarily linked to the presence of cerium, as reported in our previous studies, where both MBG3.6-Ce and MBG5.3-Ce exhibited high CAT-like activity (~90% after 30 min and 100% after 120 min) [10,11,18]. The data reveal a significant CAT-like activity across all samples. Notably, Mg-doped samples exhibit some ability to decompose H_2O_2 (52-65% after 120 min); however, only Ce/Mg-doped samples achieve complete dismutation (100%). The moderate H_2O_2 decomposition observed in Mg-containing samples lacking Ce may be associated with changes in glass dissolution behaviour, local pH, or surface reactivity induced by Mg incorporation, rather than to a true redox-mediated CAT-mimetic mechanism. The complete H_2O_2 dismutation observed only in Ce-containing compositions confirms the predominant role of reversible Ce^{3+}/Ce^{4+} cycling in catalytic activity, as well explain by *Zambon* et al. [7] Furthermore, biomolecule loading does not affect CAT-like activity, as the loaded MBGs maintain excellent performance, comparable to that of pristine materials, exceeding 74% after 120 minutes in all samples. The only exceptions are MBG3.6-F and MBG5.3-F, which exhibit CAT-like activity in the range of 55–60%.

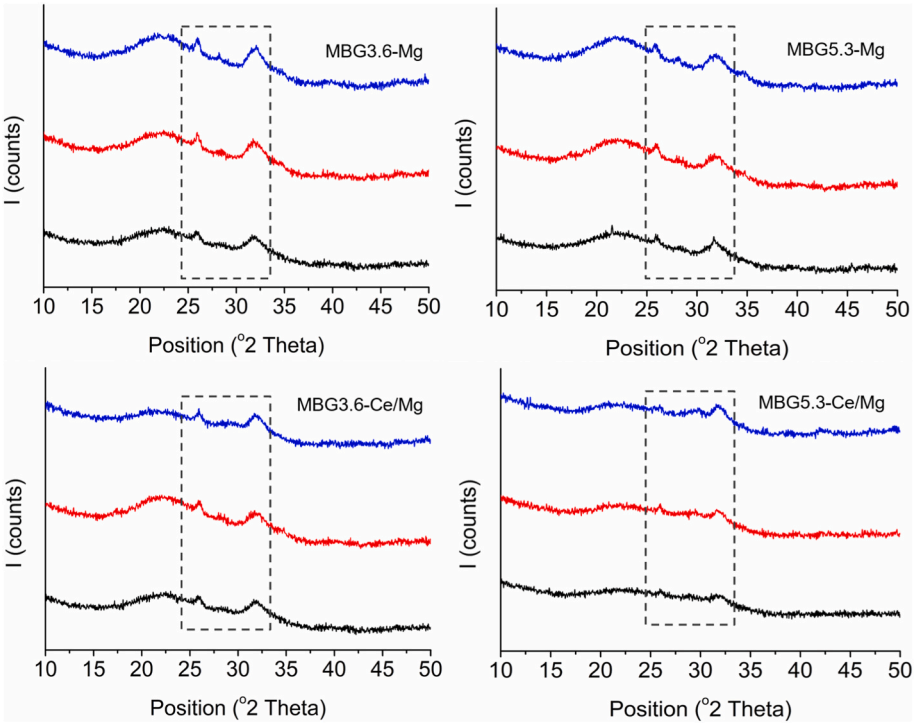

Fig. 8. XRPD patterns: MBG3.6-Mg, MBG5.3-Mg, MBG3.6-Ce/Mg, and MBG5.3-Ce/Mg after 7 (black), 14 (red), and 30 (blue) days of soaking in SBF. Black dashed line: HA.

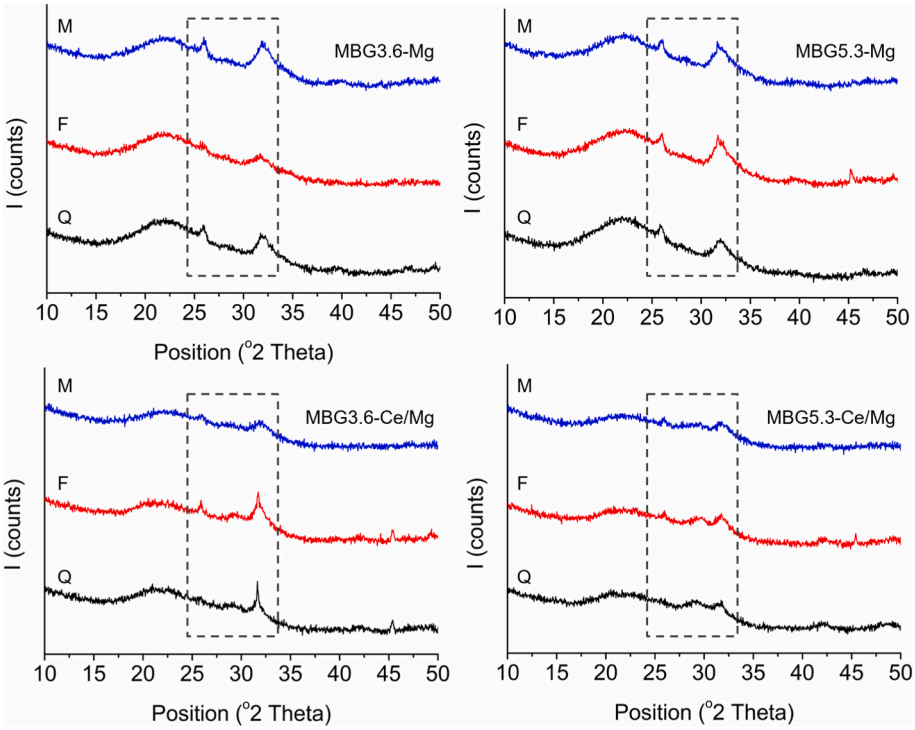

Fig. 9. XRPD patterns: MBG3.6-Mg, MBG5.3-Mg, MBG3.6-Ce/Mg, and MBG5.3-Ce/Mg, loaded with Q (black), F (red), and M (blue), after 30 days of soaking in SBF. Black dashed line: HA.

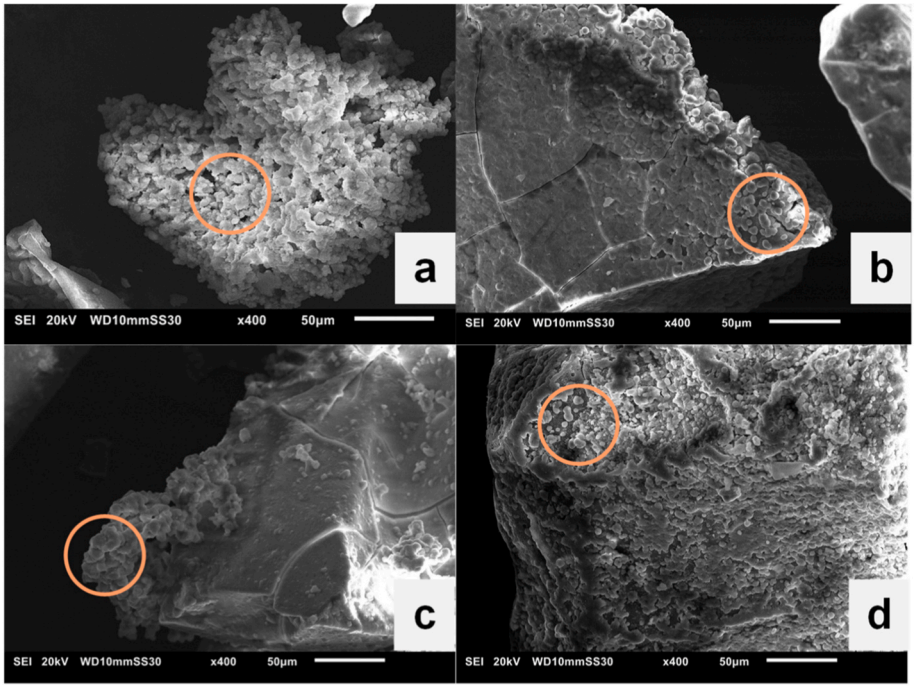

Fig. 10. SEM micrograph of MBG3.6-Mg (a), MBG3.6-Ce/Mg (b), MBG5.3-Mg (c), and MBG5.3-Ce/Mg (d) after 30 days of soaking in SBF. Red circle: HA.

3.5.2. SOD-like activity

Fig. 7 presents the SOD-like activity of MBGs and polyphenols-loaded MBGs. Our findings indicate that the SOD activity of functionalized MBGs-Ce is primarily associated with polyphenol loading, while pristine MBGs-Ce exhibit limited O_2^- scavenging ability (~20%) [10,12,18]. The results suggest that the incorporation of a second TII does not significantly influence the material's SOD-mimetic capability (~36%). All samples loaded with Q display remarkably high SOD-like activity, ranging from 83% to 97%, as expected. Conversely, F does not enhance the material's SOD activity, as its performance remains comparable to that of unloaded samples. M slightly increases SOD activity (47–61%), except for the MBG5.3-Ce/Mg sample, where no difference is observed compared to the unloaded glass.

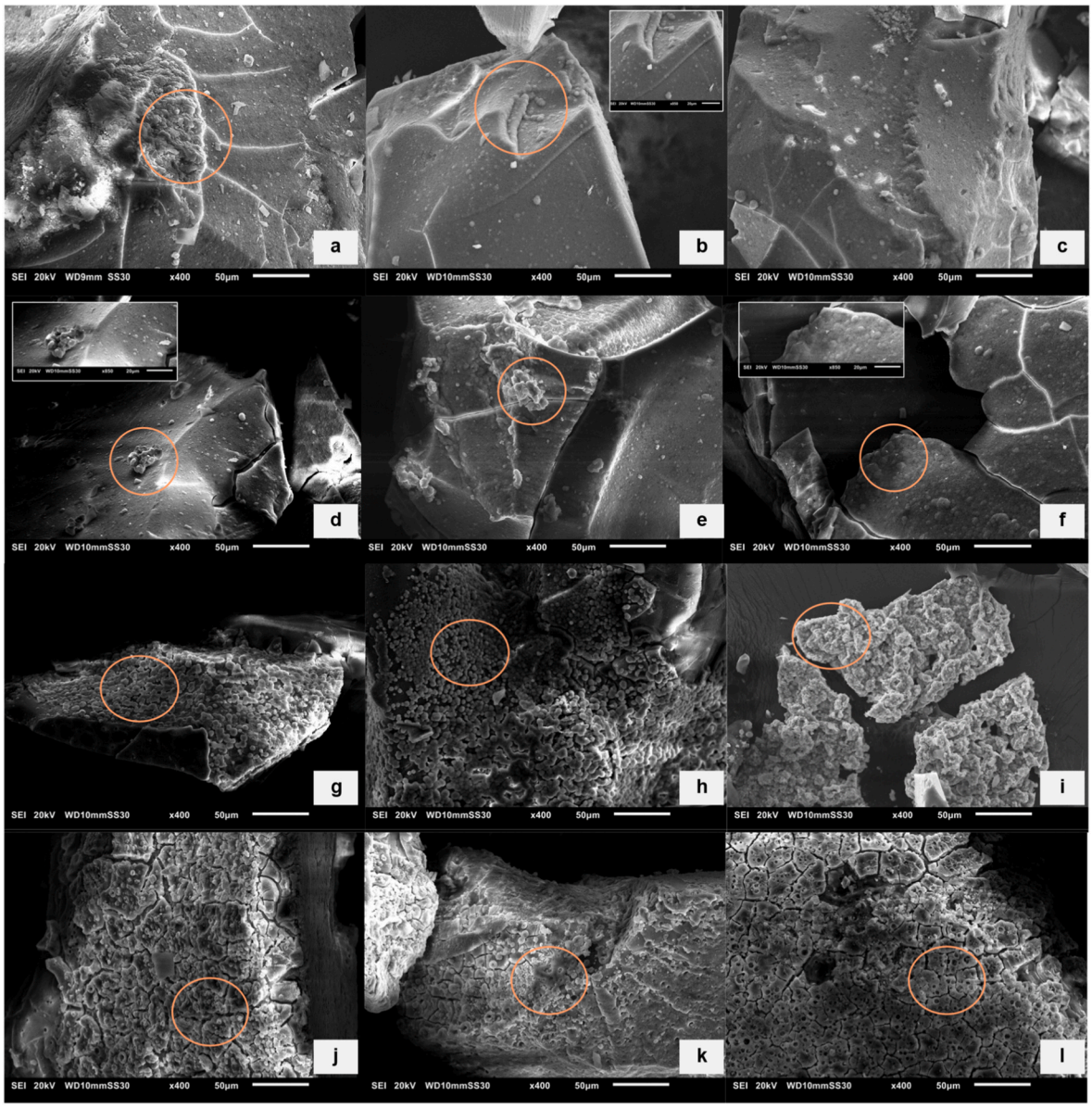

Fig. 11. SEM micrograph of MBG3.6-Mg (a-c), MBG5.3-Mg (d-f), MBG3.6-Ce/Mg (g-i) and MBG5.3-Ce/Mg (j-l), loaded with Q (a, d, g, j), F (b, e, h, k) and M (c, f, i, l), after 30 days of soaking in SBF. Scale bar 50 µm. Red circle: HA.

Table 4
Molar ratio Ca/P of MBGs3.6 and MBGs5.3 after 30 days of soaking in SBF. UL = unloaded.

MBGs	Ca/P			
	UL	Q	F	M
MBGs3.6-Mg	0.91	1.36	1.54	1.52
MBGs3.6-Ce/Mg	0.48	2.39	1.53	1.27
MBGs5.3-Mg	0.49	1.40	1.70	1.26
MBGs5.3-Ce/Mg	0.67	1.71	1.54	0.97

3.6. *In vitro bioactivity assessment*

3.6.1. *XRPD and FT-IR analyses*

Fig. 8 shows the XRPD patterns of MBG3.6-Mg, MBG5.3-Mg, MBG3.6-Ce/Mg, and MBG5.3-Ce/Mg after 7, 14, and 30 days of soaking in SBF. Characteristic HA peaks appear at 26, 32, and 33° (2θ) (JCPDS 00-009-0432) [48]. HA formation is evident in all samples after just 7 days, though bioactivity is slightly reduced in double-ion-doped samples compared to those containing only Mg. Previous studies on MBGs-Ce reported that polyphenol loading significantly slowed bioactivity [12]. However, as shown in Fig. 9, Q and F do not markedly affect the bioactivity of MBGs-Mg and MBGs-Ce/Mg, whereas the M-loaded samples exhibit a slight qualitative reduction in bioactivity. Similar results are observed in the FT-IR measurements in the Supplementary Information (Figs. S1 and S2), where the characteristic bands of HA at 605 and 565 cm^{-1} can be detected.

3.6.2. *SEM-EDS analyses*

SEM-EDS analyses (Figs. 10 and 11 and Table 4) show the presence of HA aggregates on the surface of UL MBGs and MBGs loaded with Q and F. As shown by the other analyses, also in this case, the bioactivity of the MBGs-M is slightly slowed down compared to the others.

3.7. *In vitro biological analysis of quercetin-loaded MBGs*

As summarized in Table 3, the loading efficiency and loading content varied significantly across the polyphenol-loaded MBGs. While Q, F

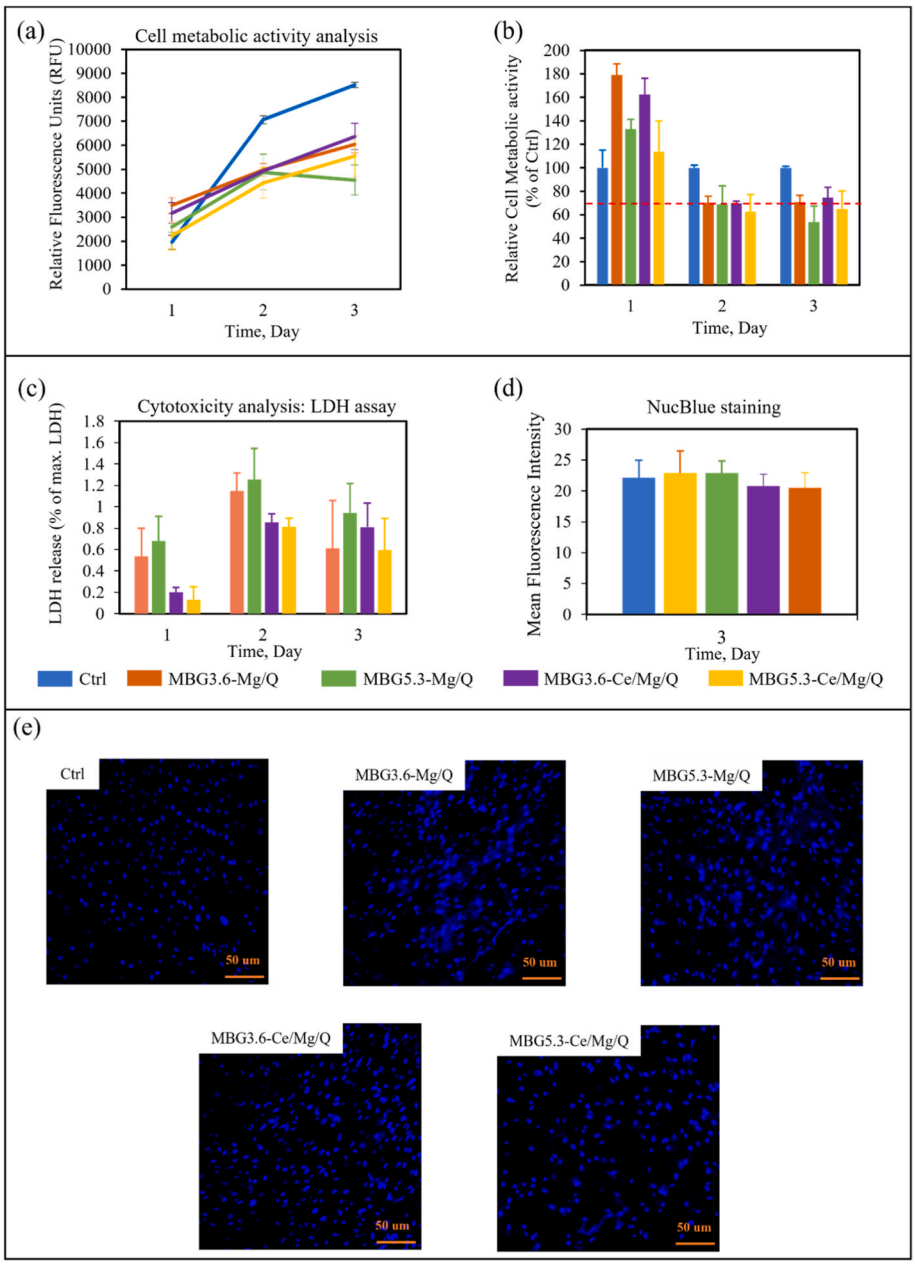

Fig. 12. *In vitro* evaluation of quercetin-loaded MBGs cultured with hBMSCs. (a) Metabolic activity assessed via Alamar Blue assay and presented as RFU and (b) normalized metabolic activity relative to control (Ctrl; untreated hBMSCs). (c) Percentage of LDH release into conditioned media normalized to the maximum LDH release for a 3-day incubation period. (d) NucBlue mean fluorescence intensity and (e) visualized NucBlue-stained nuclei of hBMSCs seeded on MBGs. Bars represent means ± SD of n = 3 replicates.

exhibited the highest loading (up to 1.3% LC), morin hydrate (M) showed a notably lower affinity for the MBG framework. However, the functional performance was most distinctive in the antioxidant assays; Q-loaded samples displayed remarkably high SOD-like activity (83-97%), section 3.5.2, whereas F-loaded samples showed no significant improvement over the unloaded controls, and M-loaded samples provided only moderate increases (47-61%).

Based on these comparative findings, quercetin-loaded MBG disks were prioritized as the lead candidate for further biological evaluation with hBMSCs. This selection was strategically made to investigate whether the high acellular antioxidant activity observed translates into functional anti-oxidant and anti-inflammatory effects within a cellular environment. Furthermore, these studies were essential to confirm that the loading process did not compromise the inherent cytocompatibility of the MBGs. Consequently, the subsequent analysis focused on the direct interaction between hBMSCs and the quercetin-loaded disks to validate their potential for regenerative medicine applications.

3.7.1. *Cytocompatibility analysis*

The cytocompatibility of quercetin-loaded MBG disks was evaluated through direct contact assays with hBMSCs, utilising metabolic activity measurements, LDH release quantification, and visual assay by nuclear staining. The relative fluorescence units (RFU) demonstrated a progressive increase over the 3-day incubation period across all experimental groups, indicating sustained cellular proliferation (Fig. 12a). Notably, the relative metabolic activity for all quercetin-loaded MBGs (Fig. 12b) remained above 70% compared to the control group, thus satisfying the biological safety requirements for biomaterials (ISO 10993-5), except MBG5.3-Mg-Q which showed a slight reduction in metabolic activity on day 3. No statistically significant differences were

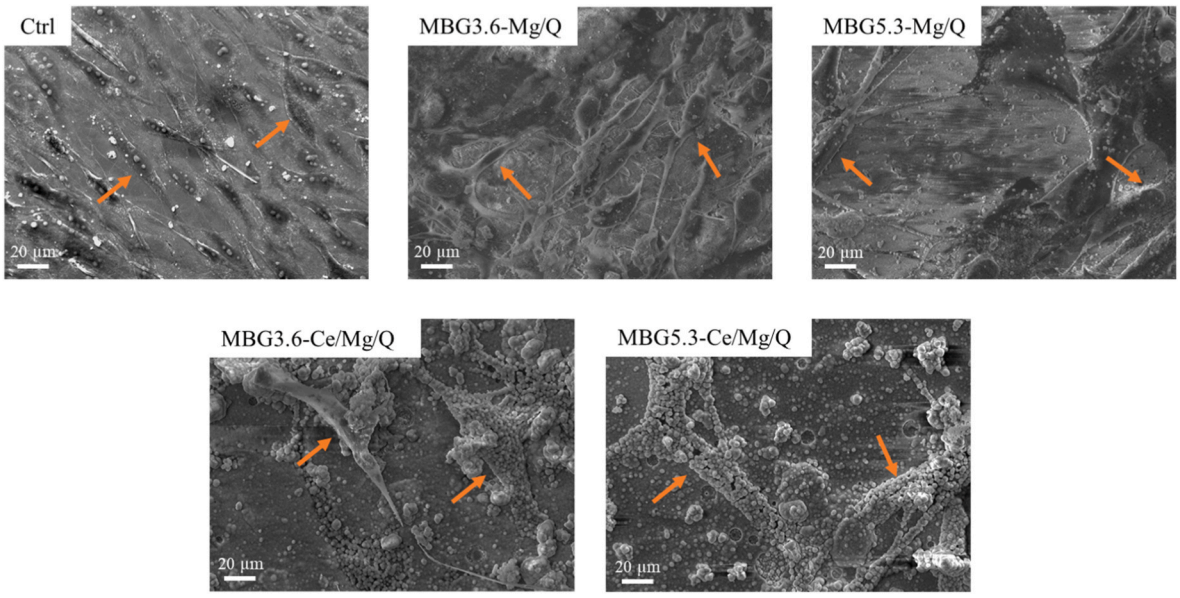

Fig. 13. Morphological evaluation of hBMSCs (indicated with orange arrows) after 3 days of culture on quercetin-loaded MBGs. SEM micrographs show cell attachment and normal phenotype. Magnification = 600x, scale bars 20 μm.

observed between the test and control groups ($p > 0.05$).

These findings were corroborated by the LDH assay (Fig. 12c), which unlike direct viability counts, measures the ratio of extracellular LDH to the total cellular LDH content (maximum release) released by dead cells due to membranes' irreversible damage. On Day 3, all the samples exhibited an LDH release of below 1.5%. This low leakage rate confirms that these disks do not compromise the cell membrane, aligning with the ISO 10993-5 requirement and further validating the inert nature of the disks. Qualitative analysis of nuclear-stained images (Fig. 12e) revealed a cell density on the quercetin-loaded MBG disks comparable to that of the control polystyrene surface (gold standard). Furthermore, quantitative assessment of the mean fluorescence intensity showed no significant deviation from the control, confirming that neither the MBG processing nor the loading of quercetin compromised the material's cytocompatibility (Fig. 12d). Collectively, these results demonstrate that the quercetin-loaded MBGs provide a favourable microenvironment for hBMSCs adhesion, spread and proliferation. These observations align with the existing literature, which suggests that the incorporation of quercetin in MBGs nanoparticles improves cytocompatibility [42,43].

The morphology of hBMSCs cultured on the MBG disks was characterized via SEM imaging. Cells in direct contact with the MBG disks exhibited a physiological, fibroblast-like morphology with no evidence of membrane damages nor apoptotic-like round shapes (Fig. 13). The hBMSCs appeared well-adherent, characterized by filopodia and the presence of cytoplasmic extensions. Notably, for the MBG3.6-Ce/Mg-Q and MBG5.3-Ce/Mg-Q compositions, granular deposits were observed across the surface. EDS confirmed that the precipitates were primarily composed of calcium (Ca) and phosphorus (P). For MBG3.6-Ce/Mg-Q, mass percentages were 48.76±0.59% for Ca and 20.62±0.25% for P; for MBG5.3-Ce/Mg-Q, values were 24.20±0.28% and 14.50±0.14%, respectively. This observation is consistent with the dissolution studies (section 3.3), which indicated higher calcium release rates for the Ce-containing samples, thereby facilitating local mineral precipitation. Detailed EDS elemental mapping and mass percentage of all the elements of the surfaces are provided in the Supplementary Information (Fig. S3).

3.7.2. Antioxidant activity

The antioxidant properties of the MBG disks were visually confirmed through fluorescence imaging, which revealed a marked reduction in green fluorescence (CellROX Green Reagent) in the MBG disks compared to the control, as shown in Fig. 14a. This significant decrease ($p<0.0001$) indicates that the quercetin-loaded MBG disks successfully protected the hBMSCs from H_2O_2-induced oxidative stress. This might be the cumulative effect of Ce and quercetin present in the sample, as Ce has redox characteristics because of its electrical structure and mimics SOD/CAT to get rid of excessive ROS inside cells. Secondly, hydroxyl groups, which can stabilize reactive species by giving the ROS a single electron or a hydrogen atom, may be the mechanism behind quercetin's ROS scavenging function [44–46]. Quantitative analysis (Fig. 14b) of the fluorescent units supported these observations; the control samples exhibited an intensity of 12.75±0.42, whereas the values for the MBG disks were substantially lower: 0.94±0.45 (MBG3.6-Mg-Q), 0.53±0.27 (MBG5.3-Mg-Q), 0.78±0.12 (MBG3.6-Ce/Mg-Q), and 2.12±1.08 (MBG5.3-Ce/Mg-Q). These biological analysis results correlate strongly with the biochemical findings detailed in Sections 3.4 and 3.5, where the quercetin-loaded MBGs demonstrated enhanced SOD-like and CAT-like mimetic activities, respectively. Collectively, these data suggest that the release of quercetin, potentially synergised by the Ce ions, effectively scavenges ROS and mitigates intracellular oxidative damage.

3.7.3. Anti-inflammatory response analysis

As expected, the expression of pro-inflammatory markers, *CXCL8* and *TNF-α*, was up-regulated up to 75.6-fold and 5.7-fold, respectively, in the positive control group when cells were stimulated with the cytokines cocktail (Fig. 15, upper panel). Interestingly, the positive control group also exhibited a 4-fold increase in *TGF-β1* expression, which likely reflects the intrinsic immunomodulatory response of hBMSCs to inflammatory stimuli [47]. In contrast, the pro-inflammatory genes were down-regulated in the quercetin-loaded MBG groups, with the exception of a moderate ($p<0.05$) *TNF-α* up-regulation (2.8-fold) in the 5.3-Mg-Q group. The observed downregulation of pro-inflammatory genes in quercetin-loaded MBGs is consistent with previous literature reporting its ability to directly tune the pro-inflammatory cascade [48]. In fact, quercetin was demonstrated to be effective in directly blocking the activation and nuclear translocation of Nuclear Factor Kappa B (NF-κB), a key signal activating the pro-inflammatory cascade [49]. As a consequence, the down-regulation of CXCL8 and TNF-α here observed is due to the fact that their promoter regions did not bind with their direct transcriptional factor NF-κB that was blocked by quercetin [50]. In

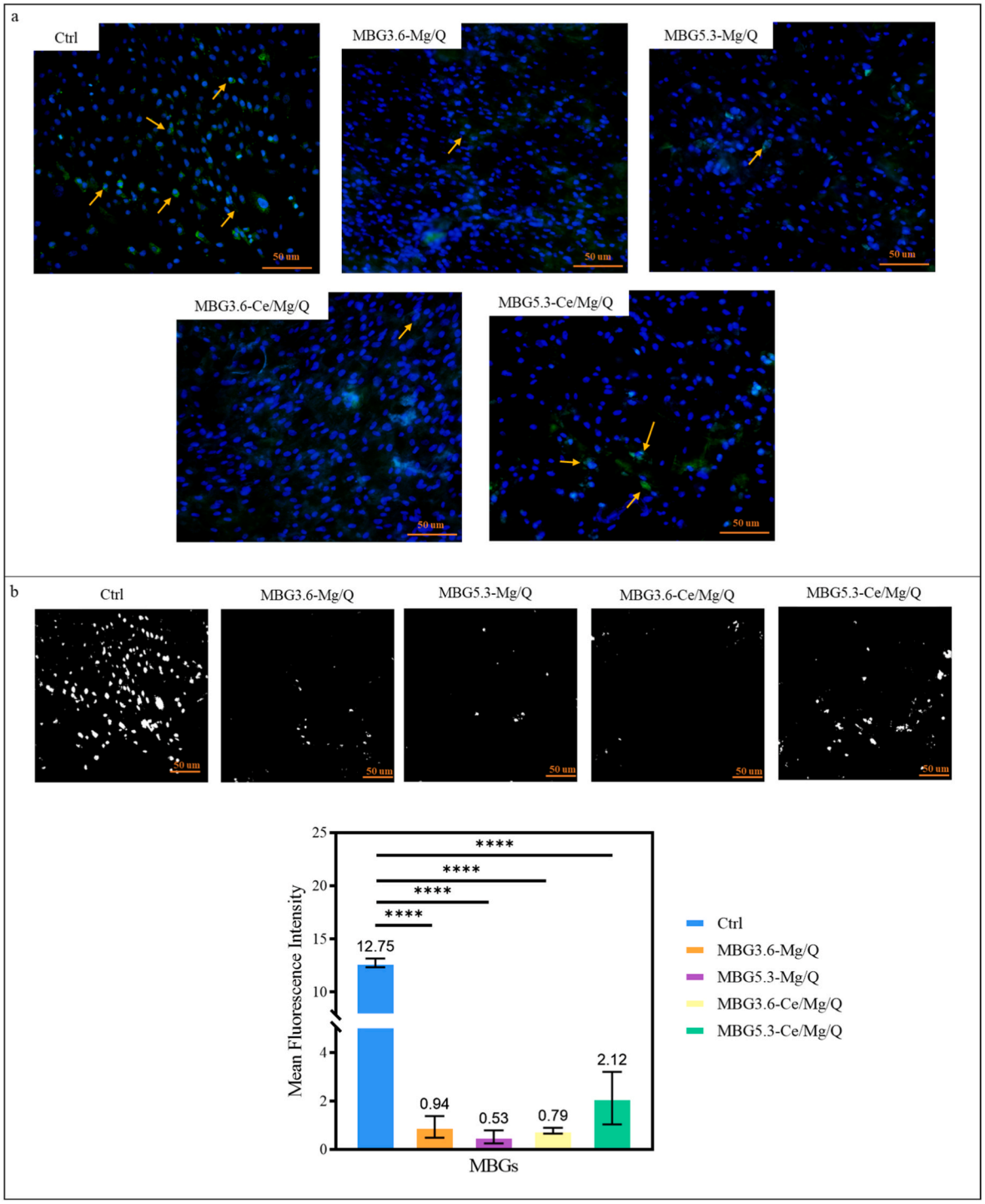

Fig. 14. Intracellular ROS accumulation in hBMSCs on MBGs under oxidative stress. (a) Representative fluorescence microscopy images of hBMSCs seeded on MBGs and incubated for 48 h under oxidative stress. ROS were visualized using CellROX Green Reagent (green) marked with yellow arrows, and nuclei were counterstained with nuclear staining (blue). (b) Quantitative analysis of intracellular ROS levels performed via ImageJ-based thresholding of green fluorescence intensity. Data are presented as mean of 3 replicates ± SD. Statistical significance relative to the control (ctrl) group is indicated as **** (= $p < 0.0001$).

particular, the 5.3-Ce/Mg-Q group demonstrated the most potent anti-inflammatory effect, with a 9.5-fold and 8.7-fold significant upregulation ($p<0.0002$) of *IL-10* and *TGF-β1,* respectively, in comparison to control. And, also among all the MBGs, it exhibited higher anti-inflammatory gene upregulation with a significant difference of $p<0.001$. These results suggest that the synergistic combination of cerium, magnesium, and quercetin within the MBG framework effectively polarises the cellular response toward an anti-inflammatory and pro-regenerative phenotype [49–51]. In fact, Ce, Mg and quercetin can exert their anti-inflammatory function through different mechanisms. Cerium contributes to the prevention of NF-κB activation: it inhibits the nuclear translocation of the p65 subunit by blocking phosphorylation [51]. Therefore, Ce exerts complementary activity to quercetin as it acts on the same target (NF-κB) but with a different mechanism. Differently, the anti-inflammatory role of magnesium is known to be related to its ability to act as a calcium channel blocker being a natural antagonist

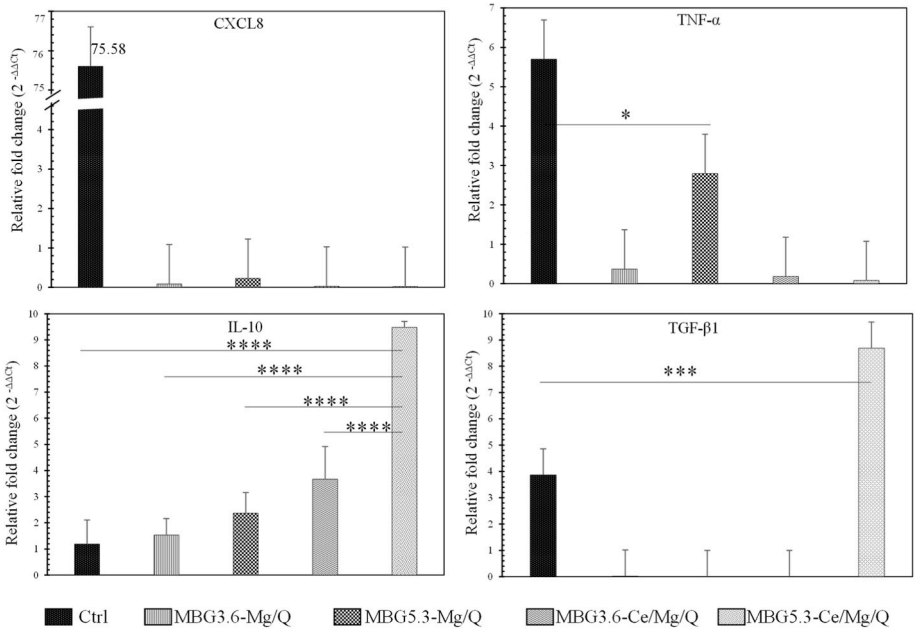

Fig. 15. Impact of MBGs on pro- and anti-inflammatory gene expression in hBMSCs. Relative fold change of pro-inflammatory (CXCL8 and TNF-α) and anti-inflammatory (I-10 and TGF-β1) genes in Ctrl versus MBG-treated groups following 48 hours of incubation under inflammatory conditions. Statistical significance is defined as $p < 0.05$ (*), $p < 0.0002$ (***), and $p < 0.0001$ (****).

[52]; in this scenario, magnesium undermines calcium for the binding site of N-methyl-D-aspartate (NMDA) receptors and L-type voltage-gated calcium channels [52]. As a result, a strong decrease in the activation of the pro-inflammatory NF-κB and Activator Protein 1 (AP1) is observed [53], as well as the NLRP3 inflammasome can not assemble due to the low calcium levels [54].

Taken together such information, it is not surprising that the MBG-Ce/Mg-Q systems resulted as the most efficient in tuning in situ the pro-inflammatory cascade over the other combinations, as they combine different mechanism in the same platform. Our results are in line with previous literature: for example, Wu et al. reported that the introduction of cerium oxide nanoparticles into magnesium-based implants improved the quality of the newly formed bone by a synergistic effect [55], confirming the possibility to enhance bioactivity by the Ce-Mg combination. Similarly, the possibility to apply MBGs as carrier for the controlled release of polyphenols was previously successfully explored by Pourshahrestani et al. [56] showing how tannic acid can be useful to counteract oxidative stress and improve wound healing, while Zhao et al. [57] reported a successful combination of MBGs and procyanidin for repairing musculoskeletal trauma. However, to the best of our knowledge, this is the first attempt involving at the same time the use of ions co-doping and polyphenols release from the same MBG platforms, thus showing a promising improvement of such systems.

4. Conclusions

This study describes the design and development of Ce-doped and Ce/Mg co-doped mesoporous bioactive glasses (MBGs) as multifunctional drug delivery systems for polyphenol loading and antioxidant enhancement. All compositions preserved the typical amorphous mesoporous structure, high specific surface area, and *in vitro* bioactivity, as confirmed by apatite formation in SBF. Importantly, the simultaneous incorporation of magnesium and cerium did not compromise the structural integrity nor the intrinsic bioactive behaviour of the glasses.

Ce/Mg co-doping significantly enhanced CAT-like activity, confirming the key role of cerium redox cycling (Ce^{3+}/Ce^{4+}) in hydrogen peroxide decomposition. Magnesium-only samples showed moderate antioxidant activity, whereas complete dismutation was achieved only in the presence of cerium. Polyphenol loading further broadened the antioxidant profile; notably, quercetin functionalization markedly improved SOD-like activity (up to 97%) without affecting CAT-like performance or bioactivity. These results highlight the complementary mechanisms of inorganic ion doping and biomolecule loading in modulating different ROS species. Quercetin-loaded Ce/Mg MBGs show the best antioxidant performance among the systems investigated.

Crucially, the antioxidant properties of the materials elicit anti-inflammatory response and reduce oxidative stress in cells. In vitro assays confirmed sustained cytocompatibility toward hBMSCs, minimal LDH release, and proper cell adhesion and spread. Under oxidative stress, quercetin-loaded disks significantly reduced intracellular ROS levels, while in a pro-inflammatory environment they promoted the upregulation of IL-10 and TGF-β1 and downregulation of pro-inflammatory mediators. The 5.3-Ce/Mg-Q composition exhibited the strongest anti-inflammatory response, underscoring the synergistic interplay among cerium, magnesium, and quercetin.

Overall, we show that therapeutic ion co-doping combined with polyphenol functionalization provides a versatile platform capable of addressing oxidative stress and inflammation—two key factors limiting tissue regeneration [58,59]. The present findings establish the antioxidant and immunomodulatory foundations of the platform and dedicated osteogenic assays are planned for the subsequent phase of investigation as they represent a current limitation of the study. These findings position Ce/Mg co-doped, quercetin-loaded MBGs as advanced multifunctional biomaterials with strong potential for regenerative medicine applications.

CRediT authorship contribution statement

Chiara Cavazzoli: Data curation, Investigation, Methodology, Validation, Writing – original draft, Writing – review & editing. **Ranveer Kaur:** Data curation, Investigation, Methodology, Validation, Writing – original draft, Writing – review & editing. **Ksenia Menshikh:** Data curation, Investigation, Methodology, Validation, Writing – original draft, Writing – review & editing. **Chiara Grassi:** Investigation, Methodology. **Alfonso Zambon:** Conceptualization, Data curation, Investigation, Methodology, Resources, Supervision, Validation,

Writing – original draft, Writing – review & editing. **Lia Rimondini:** Investigation, Methodology, Supervision, Validation. **Andrea Cochis:** Conceptualization, Data curation, Investigation, Methodology, Resources, Supervision, Validation, Writing – original draft, Writing – review & editing. **Gigliola Lusvardi:** Conceptualization, Data curation, Investigation, Methodology, Resources, Supervision, Validation, Writing – original draft, Writing – review & editing.

Declaration of competing interest

The authors declare that they have no known competing financial interests or personal relationships that could have appeared to influence the work reported in this paper.

Appendix A. Supplementary data

Supplementary data to this article can be found online at https://doi.org/10.1016/j.mtchem.2026.103789.

Data availability

Data will be made available on request.

References

[1] H. Shin, S. Jo, A.G. Mikos, Biomimetic materials for tissue engineering, Biomaterials 24 (24) (2003) 4353–4364, https://doi.org/10.1016/S0142-9612(03)00339-9.

[2] H.R. Fernandes, A. Gaddam, A. Rebelo, D. Brazete, G.E. Stan, J.M.F. Ferreira, Bioactive glasses and glass-ceramics for healthcare applications in bone regeneration and tissue engineering, Materials 11 (12) (2018), https://doi.org/10.3390/ma11122530.

[3] J. Hum, A.R. Boccaccini, Bioactive glasses as carriers for bioactive molecules and therapeutic drugs: a review, J. Mater. Sci. Mater. Med. 23 (10) (2012) 2317–2333, https://doi.org/10.1007/s10856-012-4580-z.

[4] D. Ege, K. Zheng, A.R. Boccaccini, Borate bioactive glasses (BBG): bone regeneration, wound healing applications, and future directions, ACS Appl. Bio Mater. 5 (8) (2022) 3608–3622, https://doi.org/10.1021/acsabm.2c00384.

[5] A. Obata, S. Lee, T. Kasuga, Bioactive glass materials for tissue regeneration, J. Ceram. Soc. Jpn. 130 (8) (2022) 595–604, https://doi.org/10.2109/jcersj2.22054.

[6] T. Mehrabi, A.S. Mesgar, Z. Mohammadi, Bioactive glasses: a promising therapeutic ion release strategy for enhancing wound healing, ACS Biomater. Sci. Eng. 6 (10) (2020) 5399–5430, https://doi.org/10.1021/acsbiomaterials.0c00528.

[7] A. Zambon, G. Malavasi, A. Pallini, F. Fraulini, G. Lusvardi, Cerium containing bioactive glasses: a review, ACS Biomater. Sci. Eng. 7 (9) (2021) 4388–4401, https://doi.org/10.1021/acsbiomaterials.1c00414.

[8] Z. Sun, The use of metallic elements in bone repair scaffolds, Theor. Nat. Sci. 63 (2024) 38–44, https://doi.org/10.54254/2753-8818/63/20241568.

[9] G. Lusvardi, F. Fraulini, C. Cavazzoli, A. Zambon, Evaluation of the behaviour of hydrogels containing mesoporous glasses doped with cerium and loaded with polyphenols, Ceram. Int. 50 (18) (2024) 33937–33945, https://doi.org/10.1016/j.ceramint.2024.06.213. Part B.

[10] G. Lusvardi, F. Fraulini, S. D'Addato, A. Zambon, Loading with biomolecules modulates the antioxidant activity of cerium-doped bioactive glasses, ACS Biomater. Sci. Eng. 8 (7) (2022) 2890–2898, https://doi.org/10.1021/acsbiomaterials.2c00283.

[11] F. Fraulini, S. Raimondi, F. Candeliere, R. Ranieri, A. Zambon, G. Lusvardi, Ce-MBGs loaded with gentamicin: characterization and in vitro evaluation, J. Funct. Biomater. 14 (3) (2023), https://doi.org/10.3390/jfb14030129.

[12] A. Giordana, C. Cavazzoli, F. Fraulini, P. Zardi, A. Zambon, G. Cerrato, G. Lusvardi, Evaluation of the properties of bioactive mesoporous glasses doped with cerium and loaded with polyphenols, Materials 18 (3) (2025), https://doi.org/10.3390/ma18030709.

[13] V. Nicolini, G. Malavasi, A. Zambon, F. Benedetti, G. Cerrato, S. Valeri, P. Luches, Mesoporous bioactive glasses doped with cerium: investigation over enzymatic-like mimetic activities and bioactivity, Ceram. Int. 45 (2019), https://doi.org/10.1016/j.ceramint.2019.07.080.

[14] F. Baino, S. Fiorilli, R. Mortera, B. Onida, E. Saino, L. Visai, E. Verné, C. Vitale-Brovarone, Mesoporous bioactive glass as a multifunctional system for bone regeneration and controlled drug release, J. Appl. Biomater. Funct. Mater. 10 (1) (2012) 12–21, https://doi.org/10.5301/JABFM.2012.9270.

[15] F. Baino, S. Hamzehlou, S. Kargozar, Bioactive glasses: where are we and where are we going? J. Funct. Biomater. 9 (1) (2018) https://doi.org/10.3390/jfb9010025.

[16] V. Nicolini, E. Gambuzzi, G. Malavasi, L. Menabue, M.C. Menziani, G. Lusvardi, A. Pedone, F. Benedetti, P. Luches, S. D'Addato, S. Valeri, Evidence of catalase mimetic activity in Ce3+/Ce4+ doped bioactive glasses, J. Phys. Chem. B 119 (10) (2015) 4009–4019, https://doi.org/10.1021/jp511737b.

[17] C. Leonelli, G. Lusvardi, G. Malavasi, L. Menabue, M. Tonelli, Synthesis and characterization of cerium-doped glasses and in vitro evaluation of bioactivity, J. Non-Cryst. Solids 316 (2) (2003) 198–216, https://doi.org/10.1016/S0022-3093(02)01628-9.

[18] A. Zambon, F. Fraulini, S. Raimondi, Dual loaded Ce-MBGs with bioactivity, antioxidant and antibacterial properties, Ceram. Int. 49 (2023), https://doi.org/10.1016/j.ceramint.2023.06.295.

[19] S. Raimondi, A. Zambon, R. Ranieri, F. Fraulini, A. Amaretti, M. Rossi, Investigation on the antimicrobial properties of cerium-doped bioactive glasses, J. Biomed. Mater. Res. 110 (2021), https://doi.org/10.1002/jbm.a.37289.

[20] C. Cavazzoli, F. Fraulini, V. Nicolini, P. Zardi, E. Busi, S. Raimondi, A. Zambon, G. Lusvardi, Double-ion doped mesoporous glasses: studies on stability, antibacterial and antioxidant properties, and bioactivity, Surf. Interfaces 72 (2025) 106954, https://doi.org/10.1016/j.surfin.2025.106954.

[21] S. Kargozar, P.B. Milan, M. Amoupour, F. Kermani, S. Gorgani, S. Nazarnezhad, S. Hooshmand, F. Baino, Osteogenic potential of magnesium (Mg)-Doped multicomponent bioactive glass: in vitro and in vivo animal studies, Materials 15 (1) (2022), https://doi.org/10.3390/ma15010318.

[22] W. Jahnen-Dechent, M. Ketteler, Magnesium basics, Clin. Kidney J. 5 (2012) i3–i14.

[23] R. Swaminathan, Magnesium metabolism and its disorders, Clin. Biochem. Rev. 24 (2) (2003) 47–66.

[24] M. Pelczyńska, M. Moszak, P. Bogdanski, The role of magnesium in the pathogenesis of metabolic disorders, Nutrients 14 (2022) 1714, https://doi.org/10.3390/nu14091714.

[25] A. Anand, H. Kaňková, Z. Hájovská, D. Galusek, A.R. Boccaccini, D. Galusková, Bio-response of copper–magnesium Co-Substituted mesoporous bioactive glass for bone tissue regeneration, J. Mater. Chem. B 12 (7) (2024) 1875–1891, https://doi.org/10.1039/D3TB01568H.

[26] M. Shoaib, A. Bahadur, S. Iqbal, M.M. AL-Anazy, A. Laref, M.A. Tahir, P. A. Channar, S. Noreen, M. Yasir, A. Iqbal, K.W. Ali, Magnesium doped mesoporous bioactive glass nanoparticles: a promising material for apatite formation and Mitomycin c delivery to the MG-63 cancer cells, J. Alloys Compd. 866 (2021) 159013, https://doi.org/10.1016/j.jallcom.2021.159013.

[27] Salvatori, R.; Anesi, A.; Cavazzoli, C.; Zambon, A.; Lusvardi, G. Cytocompatibility of mesoporous bioactive glasses doped with cerium and loaded with polyphenols. J. Am. Ceram. Soc. n/a (n/a), e20395. https://doi.org/https://doi.org/10.1111/jace.20395.

[28] H. Newman, Y.V. Shih, S. Varghese, Resolution of inflammation in bone regeneration: from understandings to therapeutic applications, Biomaterials 277 (2021) 121114, https://doi.org/10.1016/j.biomaterials.2021.121114.

[29] S. Goodman, M. Maruyama, Inflammation, bone healing and osteonecrosis: from bedside to bench, J. Inflamm. Res. 13 (2020) 913–923, https://doi.org/10.2147/JIR.S281941.

[30] J. Wang, C. Guo, Z. Wei, X. He, J. Kou, E. Zhou, Z. Yang, Y. Fu, Morin suppresses inflammatory cytokine expression by downregulation of nuclear Factor-KB and mitogen-activated protein kinase (MAPK) signaling pathways in lipopolysaccharide-stimulated primary bovine mammary epithelial cells, J. Dairy Sci. 99 (4) (2016) 3016–3022, https://doi.org/10.3168/jds.2015-10330.

[31] S. Ali, X. Wang, H.-C. Yan, Morin hydrate: a comprehensive review on novel natural dietary bioactive compound with versatile biological and pharmacological potential, Biomed. Pharmacother. 13 (2021) 111511, https://doi.org/10.1016/j.biopha.2021.111511.

[32] Y. Li, J. Yao, C. Han, J. Yang, M. Chaudhry, S. Wang, H. Liu, Y. Yin, Quercetin, inflammation and immunity, Nutrients 8 (2016) 167, https://doi.org/10.3390/nu8030167.

[33] B. Butun, G. Topcu, T. Ozturk, Recent advances on 3-Hydroxyflavone derivatives: structures and properties, Mini Rev. Med. Chem. 17 (2017) 1, https://doi.org/10.2174/1389557517666170425102827.

[34] V. Bertolucci, A. Ninomiya, G. Longato, L. Kaneko, N. Nonose, P.P. Scariot, L. Messias, Bioactive compounds from propolis on bone homeostasis: a narrative review, Antioxidants 14 (2025) 81, https://doi.org/10.3390/antiox14010081.

[35] G. Lusvardi, F. Sgarbi Stabellini, R. Salvatori, P2O5-Free cerium containing glasses: bioactivity and cytocompatibility evaluation, Materials 12 (19) (2019), https://doi.org/10.3390/ma12193267.

[36] K. Menshikh, A.K. Reddy, A. Cochis, F. Fraulini, A. Zambon, G. Lusvardi, L. Rimondini, Bifunctional mesoporous glasses for bone tissue engineering: biological effects of doping with cerium and polyphenols in 2D and 3D in vitro models, Biomaterials and Biosystems 14 (2024) 100095, https://doi.org/10.1016/j.bbiosy.2024.100095.

[37] I. Kovrlija, K. Menshikh, H. Abreu, A. Cochis, L. Rimondini, O. Marsan, C. Rey, C. Combes, J. Locs, D. Loca, Challenging applicability of ISO 10993-5 for calcium phosphate biomaterials evaluation: towards more accurate in vitro cytotoxicity assessment, Biomater. Adv. 160 (2024) 213866, https://doi.org/10.1016/j.bioadv.2024.213866.

[38] S. James, J. Fox, F. Afsari, J. Lee, S. Clough, C. Knight, J. Ashmore, P. Ashton, O. Preham, M. Hoogduijn, R.D.A.R. Ponzoni, Y. Hancock, M. Coles, P. Genever, Multiparameter analysis of human bone marrow stromal cells identifies distinct immunomodulatory and differentiation-competent subtypes, Stem Cell Rep. 4 (6) (2015) 1004–1015, https://doi.org/10.1016/j.stemcr.2015.05.005.

[39] S.W. Choi, J. Kim, Recent progress in autocatalytic Ceria nanoparticles-based translational research on brain diseases, ACS Appl. Nano Mater. 3 (2) (2020) 1043–1062, https://doi.org/10.1021/acsanm.9b02243.

[40] A. Görlach, E.Y. Dimova, A. Petry, A. Martínez-Ruiz, P. Hernansanz-Agustín, A. P. Rolo, C.M. Palmeira, T. Kietzmann, Reactive oxygen species, nutrition, hypoxia

and diseases: problems solved? Redox Biol. 6 (2015) 372–385, https://doi.org/10.1016/j.redox.2015.08.016.
[41] M. Valko, D. Leibfritz, J. Moncol, M.T.D. Cronin, M. Mazur, J. Telser, Free radicals and antioxidants in normal physiological functions and human disease, Int. J. Biochem. Cell Biol. 39 (1) (2007) 44–84, https://doi.org/10.1016/j.biocel.2006.07.001.
[42] T. Kokubo, H. Takadama, How useful is SBF in predicting in vivo bone bioactivity? Biomaterials 27 (2006) 2907–2915, https://doi.org/10.1016/j.biomaterials.2006.01.017.
[43] A.L.B. Maçon, T. Kim, E. Valliant, K. Goetschius, R. Brow, D. Day, A. Hoppe, A. Boccaccini, I. Kim, C. Ohtsuki, T. Kokubo, A. Osaka, M. Vallet-Regí, D. Arcos, L. Fraile, A. Salinas, A. Teixeira, Y. Vueva, R. Almeida, J. Jones, A unified in vitro evaluation for apatite-forming ability of bioactive glasses and their variants, J. Mater. Sci. Mater. Med. 26 (2015) 5403, https://doi.org/10.1007/s10856-015-5403-9.
[44] J.R. Jones, Review of bioactive glass: from hench to hybrids, Acta Biomater. 9 (1) (2013) 4457–4486, https://doi.org/10.1016/j.actbio.2012.08.023.
[45] J.P. Thielemann, F. Girgsdies, R. Schlögl, C. Hess, Pore structure and surface area of Silica SBA-15: influence of washing and Scale-Up, Beilstein J. Nanotechnol. 2 (2011) 110–118, https://doi.org/10.3762/bjnano.2.13.
[46] C. Migneco, E. Fiume, E. Verné, F. Baino, A guided walk through the world of mesoporous bioactive glasses (MBGs): fundamentals, processing, and applications, Nanomaterials 10 (12) (2020), https://doi.org/10.3390/nano10122571.
[47] N. Gómez-Cerezo, I. Izquierdo-Barba, D. Arcos, M. Vallet-Regí, Tailoring the biological response of mesoporous bioactive materials, J. Mater. Chem. B 3 (18) (2015) 3810–3819, https://doi.org/10.1039/c5tb00268k.
[48] S. Gates-Rector, T. Blanton, The powder diffraction file: a quality materials characterization database, Powder Diffr. 34 (2019) 1–9, https://doi.org/10.1017/S0885715619000812.
[49] Deepika, P.K. Maurya, Health benefits of Quercetin in age-related diseases, Molecules 27 (8) (2022), https://doi.org/10.3390/molecules27082498.
[50] K. Arkoudi, Y. Yuan, A.P. Cumine, C. Dyer, E. Busch-Nentwich, I. Bravo, Y. Feng, R. D. Knight, An NF-KB/TNF-Alpha signalling feedback loop acts to coordinate tissue regeneration and macrophage behaviour in zebrafish, npj Regen. Med. 10 (1) (2025) 27, https://doi.org/10.1038/s41536-025-00414-1.
[51] L. Yi, L. Yu, S. Chen, D. Huang, C. Yang, H. Deng, Y. Hu, H. Wang, Z. Wen, Y. Wang, Y. Tu, The regulatory mechanisms of cerium oxide nanoparticles in oxidative stress and emerging applications in refractory wound care, Front. Pharmacol. (2024) 15–2024, https://doi.org/10.3389/fphar.2024.1439960.
[52] T. Shimosawa, K. Takano, K. Ando, T. Fujita, Magnesium inhibits norepinephrine release by blocking N-Type calcium channels at peripheral sympathetic nerve endings, Hypertension 44 (6) (2004) 897–902, https://doi.org/10.1161/01.HYP.0000146536.68208.84.
[53] I.V. Savchenko, I.D. Zlotnikov, E.V. Kudryashova, Biomimetic systems involving macrophages and their potential for targeted drug delivery, Biomimetics 8 (7) (2023), https://doi.org/10.3390/biomimetics8070543.
[54] G. de Oliveira Franco, M. Romao-Veiga, V.R. Ribeiro-Vasques, P. Braga da Silva, L. R.C. de Oliveira, M.T.S. Peracoli, J.C. Peracoli, Modulatory effect of magnesium sulfate on NLRP3 inflammasome expression by human monocytes stimulated in vitro with monosodium urate, Hum. Immunol. 87 (3) (2026) 111668, https://doi.org/10.1016/j.humimm.2026.111668.
[55] G.-L. Wu, C.-E. Yen, W.-C. Hsu, M.-L. Yeh, Incorporation of cerium oxide nanoparticles into the Micro-arc oxidation layer promotes bone formation and achieves structural integrity in magnesium orthopedic implants, Acta Biomater. 191 (2025) 80–97, https://doi.org/10.1016/j.actbio.2024.11.008.
[56] S. Pourshahrestani, I. Unalan, E. Zeimaran, Z. Xu, J.A. Roether, A. Kerpes, C. Janko, C. Alexiou, A.R. Boccaccini, Tannic acid-loaded Zinc- and copper-doped mesoporous bioactive glass nanoparticles: potential antioxidant nanocarriers for wound healing, Bioact. Mater. 54 (2025) 71–85, https://doi.org/10.1016/j.bioactmat.2025.07.046.
[57] S. Zhao, Y. Jin, Z. Jia, R. Gu, Y. Ma, Y. Zhang, Y. Zhao, K. Li, Y. Xu, W. Ding, Self-assembled mesoporous bioglass polyphenol nanozymes for repairing musculoskeletal trauma, Biomaterials 333 (2026) 124153, https://doi.org/10.1016/j.biomaterials.2026.124153.
[58] W. Fabien, L. Laurent, C. Veronique, G. Jerome, W. Yohann, Oxidative stress in bone remodelling and disease, Trends Mol. Med. 15 (10) (2009) 468–477.
[59] S.C. Manolagas, M. Almeida, Gone with the Wnts:-catenin, T-Cell factor, forkhead box O, and oxidative stress in age-dependent diseases of bone, Lipid, and Glucose Metabolism (2007), https://doi.org/10.1210/me.2007-0259.